Formation of Power-law Electron Energy Spectra in Three-dimensional Low-β Magnetic Reconnection

Xiaocan Li , Fan Guo , Hui Li , Adam Stanier, and Patrick Kilian
Los Alamos National Laboratory, Los Alamos, NM 87544, USA; xiaocanli@lanl.gov
Received 2019 July 24; revised 2019 August 23; accepted 2019 September 5; published 2019 October 17

Abstract

While observations have suggested that power-law electron energy spectra are a common outcome of strong energy release during magnetic reconnection, e.g., in solar flares, kinetic simulations have not been able to provide definite evidence of power-laws in energy spectra of nonrelativistic reconnection. By means of 3D large-scale fully kinetic simulations, we study the formation of power-law electron energy spectra in nonrelativistic low-β reconnection. We find that both the global spectrum integrated over the entire domain and local spectra within individual regions of the reconnection layer have power-law tails with a spectral index $p \sim 4$ in the 3D simulation, which persist throughout the nonlinear reconnection phase until saturation. In contrast, the spectrum in the 2D simulation rapidly evolves and quickly becomes soft. We show that 3D effects such as self-generated turbulence and chaotic magnetic field lines enable the transport of high-energy electrons across the reconnection layer and allow them to access several main acceleration regions. This leads to a sustained and nearly constant acceleration rate for electrons at different energies. We construct a model that explains the observed power-law spectral index in terms of the dynamical balance between particle acceleration and escape from main acceleration regions, which are defined based upon a threshold for the curvature drift acceleration term. This result could be important for explaining the formation of power-law energy spectrum in solar flares.

Unified Astronomy Thesaurus concepts: Interplanetary particle acceleration (826); Solar magnetic reconnection (1504); Solar flares (1496); Solar corona (1483); Plasma astrophysics (1261); Space plasmas (1544)

1. Introduction

Magnetic reconnection is one of the primary mechanisms for converting magnetic energy into plasma kinetic energy and is a major possibility for accelerating nonthermal particles in various space, solar, and astrophysical plasmas (Zweibel & Yamada 2009). One remarkable example is solar flares, where observations have suggested that a large amount of energetic electrons and ions are produced during magnetic reconnection (Lin & Hudson 1976). However, the resulting energy distribution from magnetic reconnection is still a subject of major debate. While there is strong observational evidence suggesting that power-law energy distributions are a ubiquitous consequence of magnetic reconnection in solar flare conditions (Krucker et al. 2010; Oka et al. 2013, 2015; Krucker & Battaglia 2014; Gary et al. 2018), this feature has not been reproduced in self-consistent kinetic simulations in the nonrelativistic reconnection regime, limiting our ability to study the relevant physics.

Recent kinetic simulations of magnetic reconnection in the relativistic regime have shown the formation of power-law energy spectra (e.g., Guo et al. 2014, 2015, 2019; Sironi & Spitkovsky 2014; Werner et al. 2016). However, obtaining power-law distributions in the nonrelativistic regime relevant to solar flares is considerably more difficult. Most of previous simulations were carried out with plasma $\beta \sim 1$, with a limited amount of energy converted into plasma energy, in comparison to the initial plasma energy (Drake et al. 2006, 2013; Dahlin et al. 2014, 2015, 2017). While 2D simulations with low-β condition have shown strong plasma energization, the 2D magnetic field configuration traps high-energy particles in magnetic islands due to the restricted particle motion across field lines (Jokipii et al. 1993; Jones et al. 1998), and high-energy particle acceleration is nearly prohibited due to limited

access to the main acceleration regions–reconnection exhausts and the ends of magnetic islands (Li et al. 2015, 2017). We expect that self-generated turbulence in 3D reconnection (Bowers & Li 2007; Daughton et al. 2011; Liu et al. 2013; Dahlin et al. 2015, 2017; Le et al. 2018; Stanier et al. 2019) can mitigate this effect and prevent particles from being trapped in magnetic islands or flux ropes, and enable them to access multiple acceleration regions.

In this paper, we perform a 3D fully kinetic simulation of a low-β plasma to study the formation of power-law energy spectra in nonrelativistic reconnection. We observe nonthermal particle acceleration over an extended time that leads to a power-law spectrum with spectral index $p \sim 4$ and about one decade in energy extent. We show that reconnection-driven turbulence enables stronger high-energy particle acceleration by allowing particles to access several main acceleration regions, leading to nearly constant particle acceleration rate at different energies. In Section 2, we describe the simulation setup and parameters. In Section 3, we present the results on the formation of a power-law electron energy spectrum in the 3D simulations, the transport effects in the 3D simulations, and a simple model for the power-law index that provides an estimate consistent with PIC simulations. In Section 4, we discuss the conclusions and implications based on our simulation results.

2. Numerical Simulations

We carry out 2D and 3D simulations using the VPIC particle-in-cell code (Bowers et al. 2008), which solves Maxwell's equations and the relativistic Vlasov equation. Similar to our past work (Li et al. 2015, 2017, 2018a, 2019), the simulations start from a force-free current sheet with $\boldsymbol{B} = B_0 \tanh(z/\lambda)\boldsymbol{e}_x + B_0\sqrt{\mathrm{sech}^2(z/\lambda) + b_g^2}\,\boldsymbol{e}_y$, where B_0 is

the strength of the reconnecting magnetic field, b_g is the strength of the guide field B_g normalized by B_0, and λ is the half-thickness of the current sheet. We choose $\lambda = d_i$ and $b_g = 0.2$ in our simulations with a mass ratio $m_i/m_e = 25$, where $d_i = c/\omega_{\rm pi} = c/\sqrt{4\pi n_i e^2/m_i}$ is the ion inertial length. All simulations have the same Alfvén speed $v_A \equiv B_0/\sqrt{4\pi n_0 m_i} = 0.2c$ and electron beta $\beta_e \equiv 8\pi nkT_e/B_0^2 = 0.02$. The initial particle distributions are Maxwellian with uniform density n_0 and temperature $T_i = T_e = T_0$, and $kT_0 = 0.01 m_e c^2$. Electrons are set to have a bulk velocity drift U_e so that Ampere's law is satisfied. The ratio of electron plasma frequency and electron gyrofrequency $\omega_{pe}/\Omega_{ce} = 1$. The simulation domain is $[0 < x < L_x, -L_y/2 < y < L_y/2, -L_z/2 < z < L_z/2]$, where $L_x = 150 d_i$ and $L_z = 62.5 d_i$ for both simulations, and $L_y = 75 d_i$ for the 3D simulation. The domains are resolved using grids with $n_x \times n_z = 3072 \times 1280$ for both simulations, and $n_y = 1536$ for the 3D simulation. We use 150 particles per species per cell. For electric and magnetic fields, we employ periodic boundaries along the x- and y-directions and perfectly conducting boundaries along the z-direction. For particles, we employ periodic boundaries along the x- and y-directions, and reflecting boundaries along the z-direction. Initially, a long wavelength perturbation with $B_z = 0.02 B_0$ is added to induce reconnection (Birn et al. 2001).

3. Results

3.1. Turbulence and Chaotic Magnetic Fields

We focus on results from the 3D simulation and make comparison with 2D results where necessary. As the reconnection proceeds, the current sheet becomes unstable to the tearing mode instability and breaks into multiple flux ropes in the 3D simulation. These flux ropes tend to interact and merge with each other, and secondary flux ropes are continuously generated in the 3D reconnection layer. These processes lead to a turbulent reconnection layer, as shown in Figure 1(a). At $t\Omega_{ci} = 150$, three large flux ropes remain: one is in the middle of the box; the other two near the right boundary are merging. The isosurface of the current density shows a fragmented current layer, indicating that turbulence is generated (see Appendix A for the volume rendering of the current layer and the magnetic power spectrum). Starting from 20 neighboring points along a line of $2 d_i$, the magnetic field lines quickly diverge from each other as they pass through the fragmented current layer, which indicates that the magnetic field lines become chaotic. To quantify this effect, we plot in Figure 1(b) the magnetic field line exponentiation factor σ that measures the exponential rate of separation of neighboring magnetic field lines (Boozer 2012; Daughton et al. 2014; Le et al. 2018; Stanier et al. 2019). To calculate σ, we trace the magnetic field lines a distance $L_y/2$ from a grid of points at $y = -L_y/2$ to compute the displacement map $\boldsymbol{x}_0 \rightarrow \boldsymbol{x}_f$, form the Cauchy-Green deformation tensor $\mathcal{J}\mathcal{J}^T$ using the Jacobian of this map $\mathcal{J} = \nabla_{\boldsymbol{x}_0} \boldsymbol{x}_f$, and calculate σ as $\ln(\rho_{\rm max}^{1/2})$, where $\rho_{\rm max}$ is the maximum eigenvalue of the deformation tensor. Figure 1(b) shows that σ peaks at the boundary regions and becomes finite inside the reconnection layer, indicating that the magnetic field lines become chaotic. The white bar, which indicates the starting points of the field lines shown in panel (a), crosses a boundary region with large σ. This explains why the left part of

the field lines immediately separates from the right part in Figure 1(a).

During these processes, about 31% and 25% of the magnetic energy are converted into plasma kinetic energy up to $t\Omega_{ci} = 400$ in the 2D and 3D simulations, respectively. The question is then whether the resulting particle energy spectra are different between the two simulations.

3.2. Electron Energy Spectra

Figure 2(a) shows the time evolution of the global electron spectrum integrated over the entire domain in the 3D simulation with the embedded plot comparing the spectra in 2D and 3D simulations at three different time frames. The high-energy tail ($\varepsilon \in [25, 250]\varepsilon_{\rm th}$) of the spectrum evolves into a power-law $\propto \varepsilon^{-p}$ with $p \sim 4$. The power-law gradually extends to higher energies and its spectral index does not change appreciably after $120\Omega_{ci}^{-1}$ (by 0.3 until the end of the simulation $400\Omega_{ci}^{-1}$). An additional evidence of the nonthermal nature of the high-energy tail is that electrons are accelerated to much higher energies (hundreds of $\varepsilon_{\rm th}$) than the average free energy per each electron–proton pair $(B_x^2/8\pi)/n \approx 33\varepsilon_{\rm th}$, based on the reconnection inflow plasma parameters. Comparing to the 3D simulation, we find that the maximum particle energy in the 2D simulation is three times smaller and stagnates after $100\Omega_{ci}^{-1}$, which is because high-energy electrons are confined in the magnetic islands and cannot be further energized (see Section 3.3 for more discussion). This indicates that the newly converted magnetic energy is mostly used for accelerating low-energy electrons. Because of this, the electron flux piles up around tens of $\varepsilon_{\rm th}$ and the spectrum quickly becomes steeper. In addition, although the spectrum in the 2D simulation appears to have a power-law tail, earlier simulations have shown that it is actually the superposition of different thermal-like distributions in different layers of the magnetic islands (Li et al. 2017). Because of the chaotic field lines and self-generated turbulence in the 3D simulation, we expect that local electron spectra in different regions of reconnection layer to be similar. To verify this, we accumulate energy spectra for electrons in the four regions with $(2.3 d_i)^3$ each shown by white boxes in Figure 1(a). Regions 1–3 are in different regions of the flux rope at $x \sim 120 d_i$; region 4 is in the large flux at the boundary. In contrast to that in 2D simulations (e.g., Li et al. 2017), the local spectra shown in Figure 2(b) are similar in high-energy particle flux and the power-law high-energy tail $\propto \varepsilon^{-4}$. This indicates efficient particle transport and mixing due to the chaotic field lines and turbulence-induced pitch-angle scattering (see Appendix B for the low anisotropy of energetic electrons in the 3D simulation, which indicates efficient pitch-angle scattering).

3.3. The Acceleration and Transport of High-energy Electrons

To further demonstrate the transport effect, we traced particles as the simulations proceed and analyze ones that are accelerated to high energy. Figure 3 shows one electron trajectory in the 3D simulation. Note that we have shifted the trajectory once the electron crosses the boundary at $x = 150 d_i$ to make the trajectory continuous. Figure 3 shows that this electron sample five different acceleration regions. It is first energized near the X-point at $x = 75 d_i$ when it enters the reconnection region (phase 1), then streams along the magnetic field line, and gets further energized in a small flux rope at
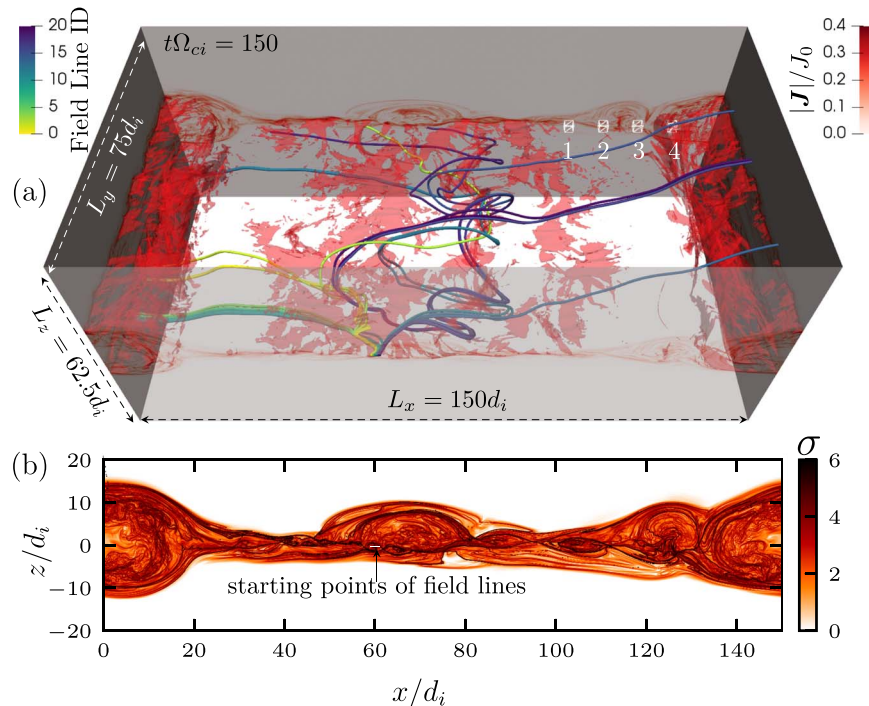
Figure 1. Turbulence and chaotic magnetic field lines in the 3D simulation. (a) 3D reconnection layer at $t\Omega_{ci} = 150$ showing the current density around the perimeter of the simulation box, an isosurface of the current density with $|J|/J_0 = 0.3$, and magnetic field lines starting from uniformly distributed points along a line of $2d_i$. The field lines are color-coded with their seed identification numbers (IDs). The white boxes of $(2.3d_i)^3$ indicate regions where the local electron energy spectra are shown in Figure 2(b). (b) Exponentiation factor σ at $t\Omega_{ci} = 150$ calculated by tracing magnetic field lines a distance $L_y/2$ from a plane of seed points at $y = -L_y/2$. The white bar indicates the starting points of the magnetic field lines shown in panel (a).

$x = 25d_i$ (phase 2). The electron is then trapped in the large flux rope at the boundary ($x \sim 150d_i$), does a typical Fermi bounce, and gets slowly energized (phase 3). Because of the chaotic field lines and self-generated turbulence, this electron manages to leave the flux rope, crosses the simulation domain, and becomes further energized in another exhaust region ($x \sim 70d_i$) (phases 4). It is then transported to $x \sim 25d_i$, where it is reflected by the mirror force, and gets energized to over $245\varepsilon_{\rm th}$ in the exhaust region at $x \sim 50d_i$. This shows how the chaotic field lines and self-generated turbulence in the 3D simulation enable particles to access multiple acceleration regions and to get further accelerated, consistent with previous results (Dahlin et al. 2015). In addition, the low plasma β condition leads to strong particle acceleration to hundreds of thermal energy.

Note that we choose this trajectory because of the clean separation between different acceleration phases, which makes it good for illustrating the idea of 3D transport. Most features described are typical in other particle trajectories, but most of them are more chaotic. We find that only a small fraction of the escaped particles can get back to the main acceleration regions.

Because of the enhanced spatial transport, high-energy electrons will be more broadly distributed in the 3D simulation. To verify this, we compare the spatial distribution of the high-energy electrons in the simulations in Figure 4. In the 2D simulation, electrons with $80\varepsilon_{\rm th} < \varepsilon < 160\varepsilon_{\rm th}$ are confined in magnetic islands and develop shells or rings (panel (a)) due to the restricted particle motion across field lines (Jokipii et al. 1993; Jones et al. 1998). As a result, these electrons cannot access the reconnection exhaust regions ($x = 20$–$50d_i$ and 75–$130d_i$), where the magnetic field is strongly bent and the energy conversion rate is the largest (Dahlin et al. 2014; Li et al. 2015, 2017). To clarify this, we plot

$v_E \cdot \kappa = (B \times \kappa/B^2) \cdot E$ in Figure 4(b), where v_E is the $E \times B$ drift velocity and $\kappa = b \cdot \nabla b$ is the magnetic curvature with b as a unit vector along the magnetic field. This term is proportional to the acceleration rate associated with particle curvature drift, which is $\varepsilon_{\parallel}(B \times \kappa/B^2)$, where $\varepsilon_{\parallel}$ is the parallel kinetic energy of a particle. Figure 4(b) shows that $v_E \cdot \kappa$ peaks at the reconnection exhaust and the two ends of a magnetic island. In contrast, in the 3D simulation, high-energy electrons are uniformly distributed in most regions of the flux ropes (panel (c)). More importantly, they are transported into the reconnection exhausts ($x = 25$–$75d_i$ and 100–$125d_i$) and the two ends of a magnetic island, so they can access the major acceleration regions similar to electrons with lower energies (panel (d)). Therefore, we expect that these electrons should have a nearly constant acceleration rate.

3.4. Particle Acceleration Rate

We use all electrons (about 590 million) in the 2D simulation and 2.5% of all electrons (about 22.6 billion) in the 3D simulation to calculate the acceleration rate $\alpha(\varepsilon) \equiv \langle \dot{\varepsilon}/\varepsilon \rangle$, where $\langle ... \rangle$ is the average for electrons in different energy bands, $\dot{\varepsilon} = -e v \cdot E$, and v is the electron velocity. Figure 5(a) shows that α peaks around $5\varepsilon_{\rm th}$ in both 2D and 3D simulations. This is because the regions, where the radius of magnetic curvature $|\kappa|^{-1} \sim d_e$ (magnetic field lines are the most strongly bent) and the acceleration rate associated with particle curvature drift ($\propto v_E \cdot \kappa$) is the strongest, are only effective at accelerating low-energy electrons ($\varepsilon < 10\varepsilon_{\rm th}$) with a gyroradius $\leqslant d_e$. For the 3D simulation, α is nearly a constant for $\varepsilon > 40\varepsilon_{\rm th}$. In contrast, α sharply decreases with particle energy and even becomes negative for some energies in the 2D simulation, which explains why the maximum energy does not change and
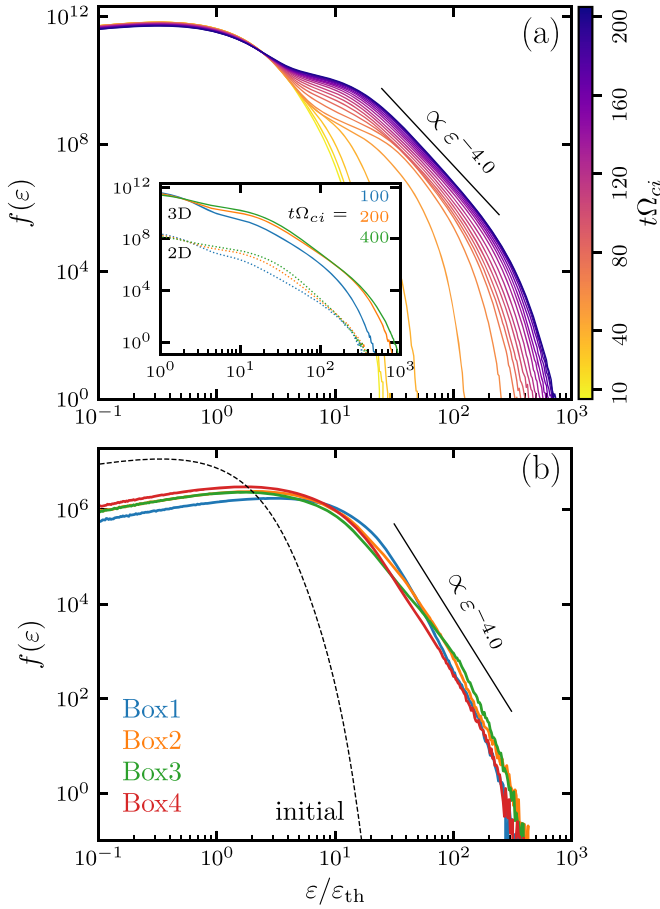
Figure 2. (a) Time evolution of the global electron energy spectrum $f(\varepsilon) = dN(\varepsilon)/d\varepsilon$ in the 3D simulation; the embedded plot compares this with the 2D simulation at three time frames. ε is the electron kinetic energy $(\gamma - 1)m_e c^2$, and γ is the Lorentz factor. We normalize ε by the initial thermal energy $\varepsilon_{\rm th} \approx 0.015 m_e c^2$. (b) Energy spectra for electrons in the four local boxes shown in Figure 1(a) at $t\Omega_{ci} = 150$.
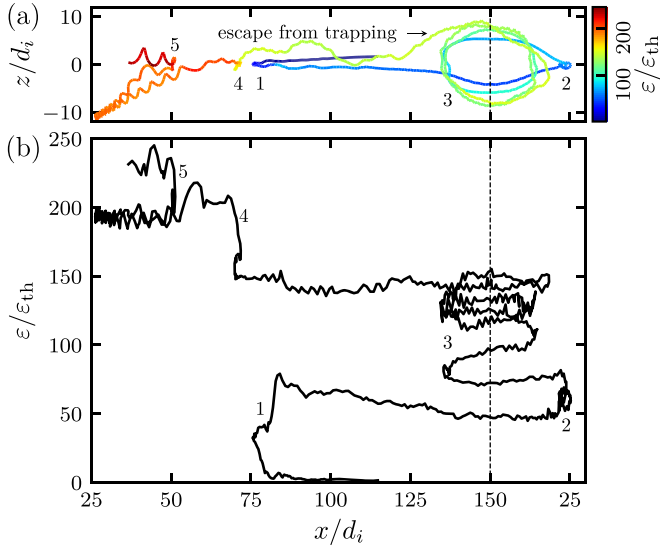
Figure 3. One electron trajectory in the 3D simulation. (a) The trajectory projected on the x–z plane and color-coded by its kinetic energy. The numbers 1–5 indicate the five phases of acceleration. The arrow points out when the electron escapes from being trapped in the large flux rope. (b) x-position vs. particle kinetic energy. Note that we have shifted the trajectory when the electron crosses the right boundary at $x = 150d_i$ (vertical dashed lines) to make the trajectory continuous.

the spectrum keeps getting steeper after $t\Omega_{ci} = 100$ in the 2D simulation. Note that $\alpha(\varepsilon)$ decreases with time as the simulation evolves in the 3D case. This is partly because the reconnection rate and energy conversion rate decrease, and because $\alpha(\varepsilon)$ is averaged for all high-energy particles but most of them are in the large flux ropes where acceleration is weak. Therefore, we need to separate particles in the major acceleration region from that in the other regions where acceleration is weak. To accomplish this, we will distinguish the major particle acceleration regions based on the acceleration mechanisms.

To reveal the acceleration mechanism, we evaluate betatron acceleration and decompose $\boldsymbol{v}$ into $\boldsymbol{v}_\parallel$ that is parallel to the local magnetic field, and the guiding-center drift velocities including curvature drift, gradient drift, inertial drift, parallel drift, and polarization drift (Northrop 1963; le Roux et al. 2015; Li et al. 2019). Figure 5(b) shows the three most important acceleration terms due to the parallel electric field (or that associated with $\boldsymbol{v}_\parallel$), associated with curvature drift, and gradient drift, respectively. Among these terms, the largest term is associated with curvature drift, consistent with previous 2D studies based on fluid quantities (Dahlin et al. 2014; Li et al. 2015, 2017) and on particles (Li et al. 2019). Figure 5(b) also shows that $\boldsymbol{E}_\parallel$ accelerates thermal particles ($\sim\varepsilon_{\rm th}$) but decelerates particles with $\varepsilon > 5\varepsilon_{\rm th}$, and that gradient drift gives deceleration for all particles. These results validate the assumption made in Figure 4 to use $\boldsymbol{v}_E \cdot \boldsymbol{\kappa}$ to separate the major acceleration region.

3.5. Model for Spectral Index

To explain the spectral index observed in the 3D simulation, we separate the main acceleration region from the rest of the reconnection layer. Particle transport into the non-acceleration region is simply treated as an "escape" effect. In order to decide the criteria for the major acceleration regions, we accumulate the PDFs of the computation cells with positive and negative $\boldsymbol{v}_E \cdot \boldsymbol{\kappa}$. The embedded plot of Figure 6(a) shows an example of the distributions at $t\Omega_{ci} = 100$. For $|\boldsymbol{v}_E \cdot \boldsymbol{\kappa}| < 0.001$, the regions with positive $\boldsymbol{v}_E \cdot \boldsymbol{\kappa}$ balances that with negative values, and the acceleration rate for particles in these regions will be $\ll 0.001$, so these regions do not contribute to the high-energy particle energization. Figure 4(d) shows that regions with positive $\boldsymbol{v}_E \cdot \boldsymbol{\kappa}$ are usually accompanied with regions with negative $\boldsymbol{v}_E \cdot \boldsymbol{\kappa}$, for example, near flux ropes at $x \sim 55d_i$ and $x \sim 90d_i$. Therefore, we choose $|\boldsymbol{v}_E \cdot \boldsymbol{\kappa}|$ around 0.001 as the threshold for separating the major acceleration regions and treat particles getting out these regions as escaped particles.

After separating the major acceleration regions, we then calculate the acceleration rate associated with curvature drift for high-energy electrons ($\varepsilon > 40\varepsilon_{\rm th}$) and their escape rate $r = 1/\tau_{\rm esc} = (dN_{\rm esc}/dt)/N_{\rm acc}$, where $N_{\rm esc}$ and $N_{\rm acc}$ are the number of high-energy electrons outside and inside the major acceleration regions, respectively. $dN_{\rm esc}/dt$ is the net effect of particle escape and re-injection at the boundaries of the main acceleration regions. For single particles (e.g., the one shown in Figure 3), there is a finite possibility that escaped particles can get back into the main acceleration regions. Statistically, more particles escape from the main acceleration regions than that are re-injected into the main acceleration regions. Figure 6(a) shows an example of the calculated rates for high-energy electrons in the major acceleration region with $|\boldsymbol{v}_E \cdot \boldsymbol{\kappa}| > 0.001$. Due to the small number of accelerated particles at the beginning of the simulation, both α and $\tau_{\rm esc}$ have a spike as reconnection starts around $30\Omega_{ci}^{-1}$. As more
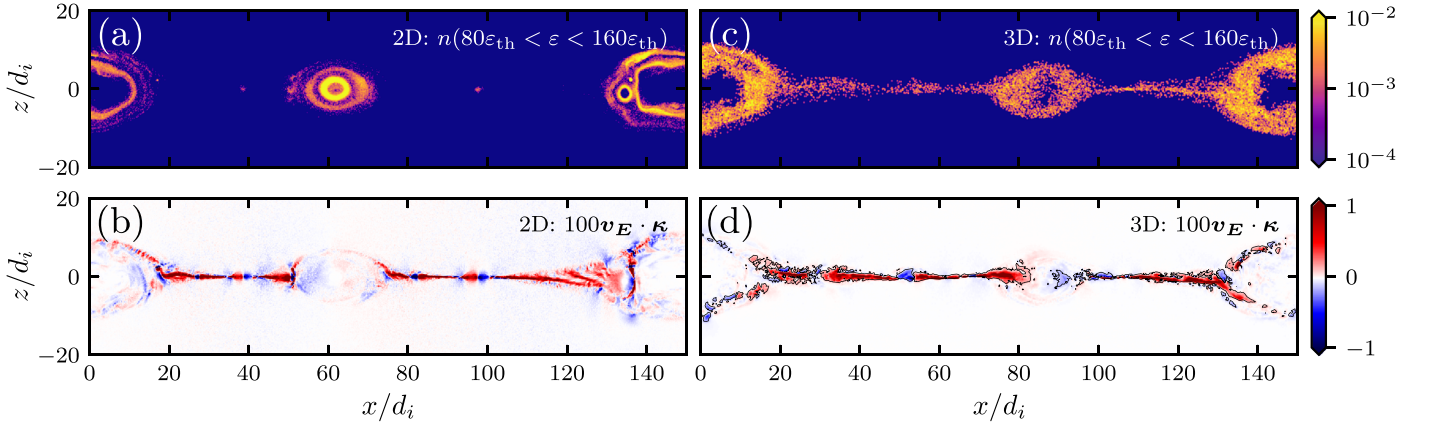
Figure 4. Spatial transport of high-energy electrons. (a) The spatial distribution of electrons with $80\varepsilon_{th} < \varepsilon < 160\varepsilon_{th}$ at $t\Omega_{ci} = 150$ in the 2D simulation. (b) $100v_E \cdot \kappa$ at $t\Omega_{ci} = 150$ in the 2D simulation, where v_E is the $E \times B$ drift velocity and κ is the magnetic curvature. (c) A y-slice ($y = 5.5d_i$) of the spatial distribution of electrons with $80\varepsilon_{th} < \varepsilon < 160\varepsilon_{th}$ at $t\Omega_{ci} = 150$. (d) A y-slice of $100v_E \cdot \kappa$ at the same y-location as panel (c). The black contour is at $|v_E \cdot \kappa| = 0.001$, indicating the boundary of the major acceleration regions. Note that the void at the boundary is caused by the initial perturbation (Birn et al. 2001).
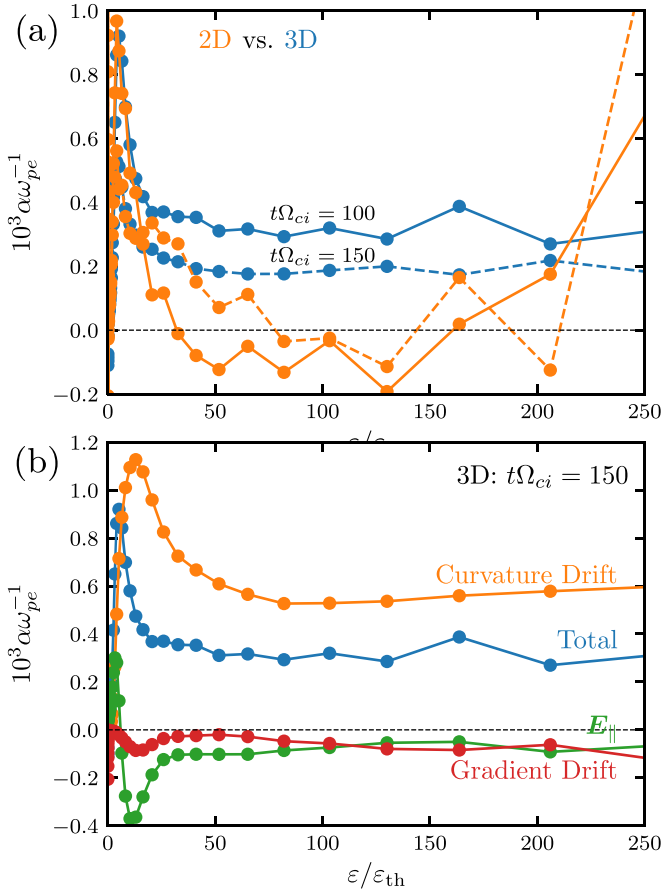
Figure 5. Diagnostics on the Fermi-type acceleration mechanism. (a) Electron acceleration rate $\alpha(\varepsilon) \equiv \langle \dot{\varepsilon}/\varepsilon \rangle$ for the 2D (orange) and 3D (blue) simulations at $t\Omega_{ci} = 100$ (solid) and 150 (dashed), where $\langle...\rangle$ is done for electrons in different energy bands, $\dot{\varepsilon} = -e\mathbf{v} \cdot \mathbf{E}$, and $\mathbf{v}$ is the electron velocity. Due to the small number of high-energy electrons, α peaks and fluctuates strongly at high energies in the 2D simulation. We have run another 2D simulation with 1500 particles/cell/species and found that the fluctuation level decreases and α at high energies is much smaller in the 2D simulation. (b) Electron acceleration associated with curvature drift, gradient drift, and the parallel electric field in the 3D simulation at $t\Omega_{ci} = 150$.
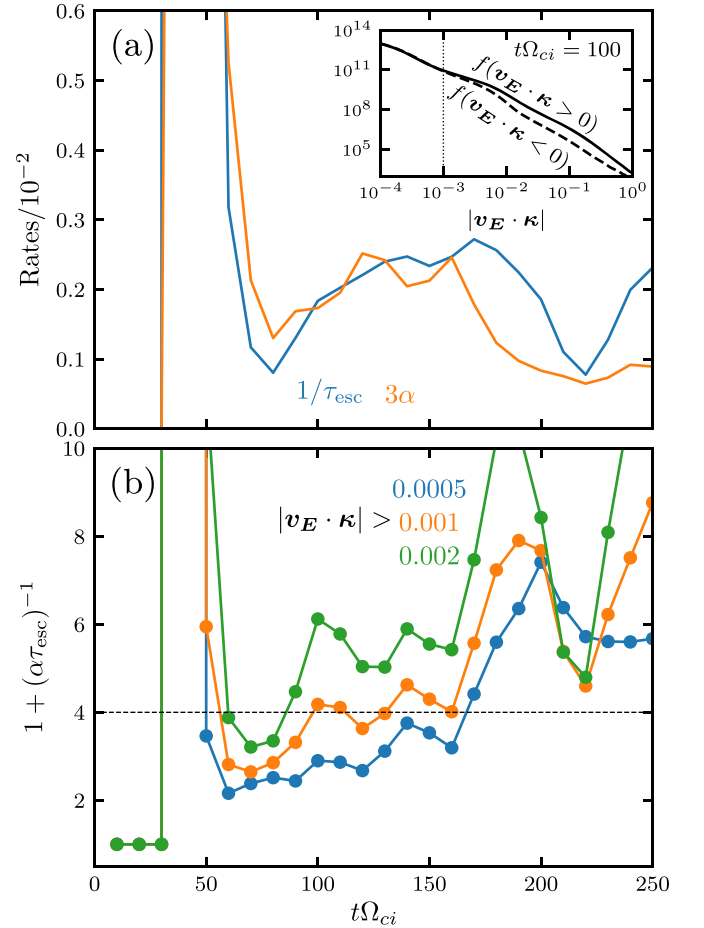
Figure 6. An estimate of the power-law index by evaluating the acceleration rate α and the escape rate $1/\tau_{esc}$ for high-energy electrons ($\varepsilon > 40\varepsilon_{th}$) in the major acceleration region, where $|v_E \cdot \kappa|$ is larger than a threshold, as indicated in Figure 4(c). (a) Time evolution of 3α and $1/\tau_{esc}$ when $|v_E \cdot \kappa| > 0.001$. The embedded plot compares the distributions of the regions with negative and positive $v_E \cdot \kappa$ at $t\Omega_{ci} = 100$. The vertical dashed line indicates the chosen threshold 0.001 for $|v_E \cdot \kappa|$. (b) The estimated power-law index for a Fermi-type acceleration mechanism $1 + (\alpha\tau_{esc})^{-1}$ for three thresholds for $|v_E \cdot \kappa|$. The dashed line indicate a power-law index 4, as obtained in the 3D simulation.

particles are accelerated, we find that $1/\tau_{esc}$ approaches 3α until $150\Omega_{ci}^{-1}$, when α sharply decreases due to the boundary condition. As a result, the power-law index for a Fermi-type

acceleration mechanism (Drury 1983; Guo et al. 2014) $1 + (\alpha\tau_{esc})^{-1}$ is about 4 before $150\Omega_{ci}^{-1}$ but suddenly increases to over 6 after that, as shown in Figure 6(b) (orange line). The values fluctuate around 4 because it is difficult to decide the escape boundary of the major acceleration region in such a turbulent system. And note that the estimated power-law index is for high-energy electrons inside the major acceleration region, while the global spectrum shown in Figure 2 is for all electrons, including that in the major acceleration region and the escaped electrons. The power-law index of the global spectrum is a dynamical balance between particle acceleration and escape. We have tried different thresholds for $|\nu_E \cdot \kappa|$. Figure 6(b) shows that the power-law index increases when the threshold is higher.

4. Discussions and Conclusions

By means of self-consistent kinetic simulations, we study the formation of power-law energy spectra in nonrelativistic low-β reconnection. We find that electrons in the 3D simulation develop a power-law tail with a power-law index $p \sim 4$. In contrast, the spectrum in the corresponding 2D simulation quickly becomes steeper as the simulation proceeds. We show that the 3D effects such as self-generated turbulence and chaotic magnetic field lines enable high-energy electrons to access several major acceleration regions, leading to a nearly constant acceleration rate for electrons at different energies. This enables the power-law tail to survive and extend to higher energy in the 3D simulation. In contrast, most high-energy electrons in the 2D simulation are slowly accelerated because they are confined in magnetic islands and cannot access main acceleration regions. As a result, newly converted magnetic energy is mostly used to accelerate low-energy electrons and the spectrum quickly becomes steeper in the 2D simulation. The 3D effects also enable electrons to be efficiently mixed, leading to nonthermal local particle distributions rather than the thermal-like distributions trapped in different layers of a magnetic island in 2D simulations (Li et al. 2017). Although the 3D effects have been studied previously in terms of reconnection dynamics (Daughton et al. 2011; Liu et al. 2013; Daughton et al. 2014; Le et al. 2018; Stanier et al. 2019) and electron energization (Dahlin et al. 2015, 2017), for the first time, we show that they are essential for the formation of power-law energy spectrum in nonrelativistic reconnection.

To explain the power-law index, we separate the acceleration region from non-acceleration regions and calculate the electron acceleration rate α and escape rate $r = 1/\tau_{esc}$ for electrons inside the acceleration region. The resulted power-law index that uses Fermi acceleration formula $p = 1 + (\alpha\tau_{esc})^{-1}$ (Drury 1983; Guo et al. 2014) fluctuates around 4, consistent with the simulation result. This shows that the electron power-law energy spectrum is a dynamical balance between acceleration and escape, as in the classical Fermi-type acceleration processes. Several comprehensive models have been developed for studying particle acceleration in nonrelativistic reconnection (Drake et al. 2006, 2013, 2019; Zank et al. 2014, 2015; le Roux et al. 2015, 2016, 2018; Montag et al. 2017; Li et al. 2018b; Zhao et al. 2018, 2019; Adhikari et al. 2019), and they all predict the formation of power-law energy distributions in certain regimes. The new 3D simulations allow us to study power-laws in nonrelativistic studies and provide opportunities for testing those models. We defer this work to a future study.

The simulation boundary conditions could play a role in the formation of power-law spectrum. The embedded plot of Figure 2(a) shows a pileup of fluxes fluxes around $20\varepsilon_{th}$ after $200\Omega_{ci}^{-1}$, resulting a steeper spectrum with $p = 4.35$ at $400\Omega_{ci}^{-1}$. This is likely caused by the periodic boundary condition employed in the simulations, which terminates the acceleration of most high-energy electrons that are in the flux rope at the boundary by slowing down the reconnection outflows after $200\Omega_{ci}^{-1}$ (see a discussion on the effect of the periodic boundary condition on energy conversion at the end of Appendix A). A simulation with more realistic open boundary conditions enables particles to escape from the boundaries and hence might lead to a steeper power-law spectrum (Guo et al. 2014). We defer the work on simulation boundary conditions to a future study.

We expect that the obtained power-law spectrum might change with simulation parameters. A larger simulation domain will allow the power-law to extend to higher energies. A lower (higher) plasma β could make the spectrum harder (softer) by increasing (decreasing) the acceleration rate. While we have shown here that power-law spectrum can be obtained in the low-β reconnection regime over the simulation timescale, our results do not rule out the possibility of generating power-law energy spectra in high-β reconnection. To develop a relatively well-defined power-law spectrum (e.g., a decade in energy extent), the acceleration has to be strong and/or last for a long time. A criterion can be that $\alpha\tau_{inj}$ should be at least a few (Guo et al. 2014, 2015), where τ_{inj} is the particle injection time from the reconnection inflow. Note that τ_{inj} is not just the simulation time because the boundary condition will play an important role in a small-scale simulation. Since the acceleration rate α is typically smaller in high-β reconnection due to a limited amount of free magnetic energy (e.g., Dahlin et al. 2017), we anticipate that a much larger simulation and longer simulation time are required in order to obtain a power-law energy spectrum in high-β reconnection.

Our 2D simulation shows that the fluxes are piled up at tens of ε_{th}, indicating that electrons are heated up to tens of ε_{th}. According to Shay et al. (2014) and Haggerty et al. (2015), the degree of electron heating in reconnection scales as $0.033m_i v_A^2$, which is $2.2\varepsilon_{th}$ based on our simulation parameters. This is much smaller than the electron heating in our simulations. The difference could be caused by different simulation setup. We use a force-free current sheet in which the plasma is uniform, and they used a Harris current sheet in which the current sheet plasma is different from the background plasma. There are multiple X-points and magnetic islands in our simulations and there is one X-point and occasional secondary islands in their simulations. The collapse of the X-points and the coalescence of the islands will further accelerate electrons and heat the plasma (e.g., Drake et al. 2013). To find out which factor determines the difference, we need to perform a series of new simulations. We defer this study to a future work.

Our simulations have a few limitations. First, we only perform simulations with a weak guide field $0.2B_0$. In reconnection with a higher guide field, the particle acceleration rate will become smaller, the dominant electron acceleration mechanism will change to be the parallel electric field (Dahlin et al. 2014, 2016; Li et al. 2015, 2017; Wang et al. 2016), and the electron heating will be due to phase mixing in the strong guide-field regime in a weakly collisional plasma (Numata & Loureiro 2015). This will change the amplitude of the

acceleration rate and its energy dependence, which might lead to different energy spectrum. Second, we perform the simulations with a low mass ratio $m_i/m_e = 25$. Our recent 2D simulations with different mass ratios have shown that the electron acceleration rate decreases with the mass ratio (Li et al. 2019). If this conclusion holds in 3D simulations, we expect a steeper spectrum than that obtained in this paper. Demonstrating this in 3D simulations with high mass ratios demands much more computation resources than that are currently available. These problems all require further studies in order to give quantitative predictions for the particle energy spectrum in a large-scale reconnection layer, e.g., solar flares.

To conclude, we study the formation of power-law electron energy spectrum in nonrelativistic low-β reconnection through performing both 2D and 3D fully kinetic simulations. We find that both the global spectrum integrated over the entire domain and local spectra within individual regions of the reconnection layer have a power-law tail with a power-law index $p \sim 4$ in the 3D simulation. In contrast, the spectrum in the 2D simulation keeps getting steeper. We show that the self-generated turbulence and chaotic magnetic field lines in the 3D simulation enable high-energy electrons transport across the reconnection layer enable them to access several main acceleration regions. This leads to a nearly constant accelera-tion rate for electrons at different energies. To explain the power-law index, we identify the major acceleration region where the acceleration associated with particle curvature drift is strong, and calculate the electron acceleration rate α and escape rate $r = 1/\tau_{\rm esc}$. The resulted power-law index that uses Fermi acceleration formula $p = 1 + (\alpha\tau_{\rm esc})^{-1}$ fluctuates around 4, consistent with the simulation result. This shows that the electron power-law energy spectrum is a dynamical balance between acceleration and escape, as in the classical Fermi-type acceleration processes. These results could be important for explaining the formation of power-law energy spectra in nonrelativistic plasmas, e.g., solar flares.

Appendix A
Additional Evidence for Self-generated Turbulence

Figure 7 shows the volume rendering of the current density in the 3D simulation $t\Omega_{ci} = 80$ and 200. At $t\Omega_{ci} = 80$, the reconnection layer is filled with flux ropes. A slice through these flux ropes shows structures that appear to be magnetic islands, but the system is actually more complicated. These flux
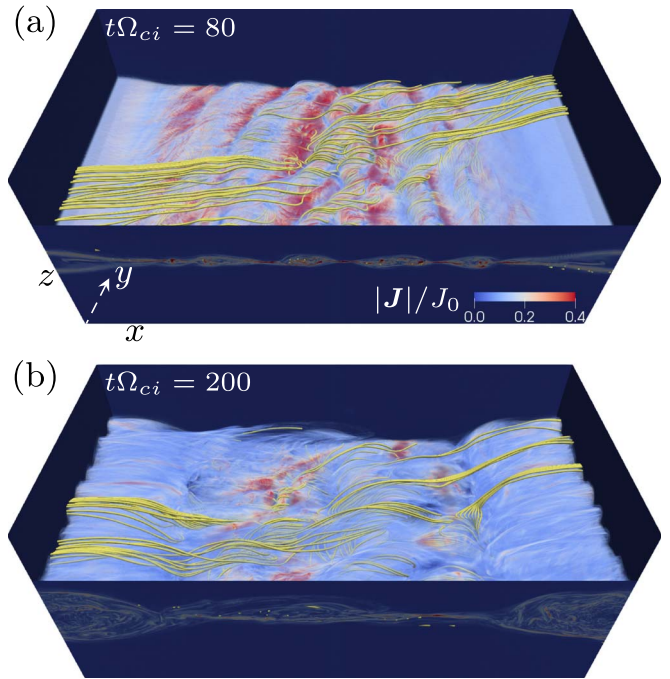

Figure 7. Volume rendering of the current density in the 3D simulation $t\Omega_{ci} =$ (a) 80 and (b) 200. Yellow lines indicate sample magnetic field lines.
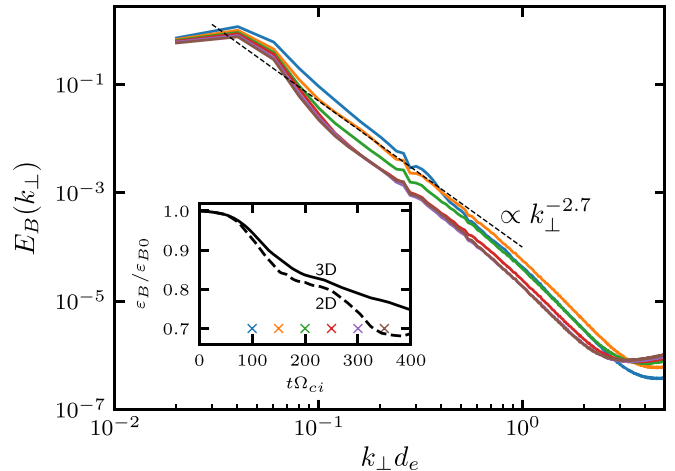

Figure 8. Magnetic power spectra at five time frames indicated by the crosses in the embedded plot. The black dashed line indicates a power-law $\propto k_\perp^{-2.7}$. The embedded plot also shows the time evolution of the magnetic energy ε_B for both simulations. ε_{B0} is the initial magnetic energy.

ropes tend to kink and interact and merge with each other, and secondary flux ropes are continuously generated in the layer. As the system evolves to $t\Omega_{ci} = 200$, only one large flux rope is left (besides the one at the boundary) because of the merging of the flux ropes, and the reconnection layer becomes even more turbulent.

We then verify the generation of turbulence by calculating the magnetic power spectrum. We subtract $B_g = 0.2B_0$ from B_y, apply a Blackman window along the z-direction, and choose the guide-field direction as the parallel direction. Figure 8 shows that the magnetic power spectrum develops a power-law $\propto k_\perp^{-2.7}$ at large scales ($k_\perp d_e < 0.3$) after $t\Omega_{ci} = 100$ and gradually steepens at small scales.

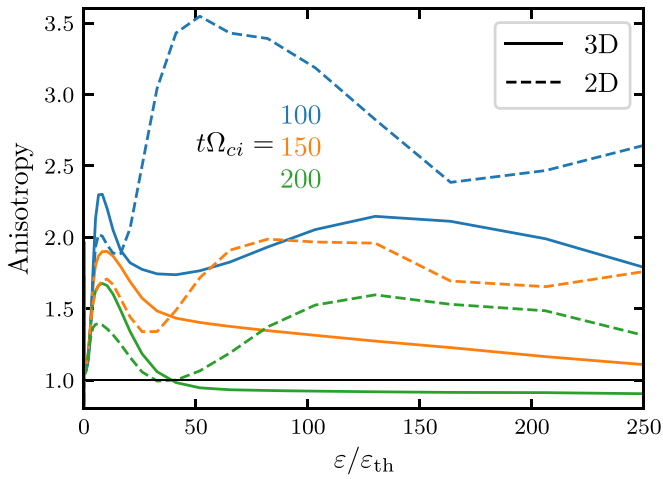The embedded plot in Figure 8 shows that the energy conversion features two fast phases with a slow phase in

Figure 9. Anisotropy of electrons at different energies. Here, the anisotropy is defined as $\Delta p_{e\parallel}/\Delta p_{e\perp}$ for different energy bands, where $\Delta p_{e\parallel} = \sum (\boldsymbol{v}_\parallel - \boldsymbol{v}_{e\parallel}) \cdot (\boldsymbol{p}_\parallel - \boldsymbol{p}_{e\parallel}/n_e)$ and $\Delta p_{e\perp} = 0.5\sum (\boldsymbol{v}_\perp - \boldsymbol{v}_{e\perp}) \cdot (\boldsymbol{p}_\perp - \boldsymbol{p}_{e\perp}/n_e)$ are the contributions of the electrons at different energy band to the parallel and perpendicular pressure, respectively. $\boldsymbol{v}_\parallel$ and $\boldsymbol{v}_\perp$ are the electron parallel and perpendicular velocity, respectively. $\boldsymbol{p}_\parallel$ and $\boldsymbol{p}_\perp$ are the electron parallel and perpendicular momentum, respectively. n_e is the electron number density. $\boldsymbol{v}_{e\parallel}$ and $\boldsymbol{v}_{e\perp}$ are the electron parallel and perpendicular flow velocities, respectively. $\boldsymbol{p}_{e\parallel}$ and $\boldsymbol{p}_{e\perp}$ are the electron parallel and perpendicular momentum density, respectively.

between for the 2D simulation, and a fast phase followed by a long slow phase in the 3D simulation. The fast to slow transition occurs when the reconnection outflows collide at the periodic boundary along the x-direction, which slows down the outflows and hence reduces the motional electric field that accelerates most particles.

Appendix B
Anisotropy of Electrons at Different Energies

To show the effect of pitch-angle scattering due to self-generated turbulence in 3D reconnection, we calculate the anisotropy of electrons at different energies and show the result at 3 time frames in Figure 9. As reconnection proceeds, the anisotropy level decreases in both 2D and 3D simulations. Comparing 2D results with 3D results, we find that the anisotropy of energetic electrons is weaker in the 3D simulation than that in the 2D simulation. At $t\Omega_{ci} = 200$, the anisotropy of energetic electrons in the 3D simulation is close to 1. These results suggest that the self-generated turbulence in 3D reconnection can scatter energetic electrons and leads to nearly isotropic electron distributions.

ORCID iDs

Xiaocan Li ● https://orcid.org/0000-0001-5278-8029
Fan Guo ● https://orcid.org/0000-0003-4315-3755
Hui Li ● https://orcid.org/0000-0003-3556-6568

References

Adhikari, L., Khabarova, O., Zank, G. P., & Zhao, L. L. 2019, ApJ, 873, 72
Birn, J., Drake, J. F., Shay, M. A., et al. 2001, JGR, 106, 3715
Boozer, A. H. 2012, PhPl, 19, 112901
Bowers, K., & Li, H. 2007, PhRvL, 98, 035002
Bowers, K. J., Albright, B. J., Yin, L., Bergen, B., & Kwan, T. J. T. 2008, PhPl, 15, 055703
Dahlin, J. T., Drake, J. F., & Swisdak, M. 2014, PhPl, 21, 092304
Dahlin, J. T., Drake, J. F., & Swisdak, M. 2015, PhPl, 22, 100704
Dahlin, J. T., Drake, J. F., & Swisdak, M. 2016, PhPl, 23, 120704
Dahlin, J. T., Drake, J. F., & Swisdak, M. 2017, PhPl, 24, 092110
Daughton, W., Nakamura, T. K. M., Karimabadi, H., Roytershteyn, V., & Loring, B. 2014, PhPl, 21, 052307
Daughton, W., Roytershteyn, V., Karimabadi, H., et al. 2011, NatPh, 7, 539
Drake, J. F., Arnold, H., Swisdak, M., & Dahlin, J. T. 2019, PhPl, 26, 012901
Drake, J. F., Swisdak, M., Che, H., & Shay, M. A. 2006, Natur, 443, 553
Drake, J. F., Swisdak, M., & Fermo, R. 2013, ApJL, 763, L5
Drury, L. O. 1983, RPPh, 46, 973
Gary, D. E., Chen, B., Dennis, B. R., et al. 2018, ApJ, 863, 83
Guo, F., Li, H., Daughton, W., & Liu, Y.-H. 2014, PhRvL, 113, 155005
Guo, F., Li, X., Daughton, W., et al. 2019, ApJL, 879, L23
Guo, F., Liu, Y.-H., Daughton, W., & Li, H. 2015, ApJ, 806, 167
Haggerty, C. C., Shay, M. A., Drake, J. F., Phan, T. D., & McHugh, C. T. 2015, GeoRL, 42, 9657
Jokipii, J. R., Kota, J., & Giacalone, J. 1993, GeoRL, 20, 1759
Jones, F. C., Jokipii, J. R., & Baring, M. G. 1998, ApJ, 509, 238
Krucker, S., & Battaglia, M. 2014, ApJ, 780, 107
Krucker, S., Hudson, H. S., Glesener, L., et al. 2010, ApJ, 714, 1108
Le, A., Daughton, W., Ohia, O., et al. 2018, PhPl, 25, 062103
le Roux, J. A., Zank, G. P., & Khabarova, O. V. 2018, ApJ, 864, 158
le Roux, J. A., Zank, G. P., Webb, G. M., & Khabarova, O. 2015, ApJ, 801, 112
le Roux, J. A., Zank, G. P., Webb, G. M., & Khabarova, O. V. 2016, ApJ, 827, 47
Li, X., Guo, F., & Li, H. 2019, ApJ, 879, 5
Li, X., Guo, F., Li, H., & Birn, J. 2018a, ApJ, 855, 80
Li, X., Guo, F., Li, H., & Li, G. 2015, ApJL, 811, L24
Li, X., Guo, F., Li, H., & Li, G. 2017, ApJ, 843, 21
Li, X., Guo, F., Li, H., & Li, S. 2018b, ApJ, 866, 4
Lin, R. P., & Hudson, H. S. 1976, SoPh, 50, 153
Liu, Y.-H., Daughton, W., Karimabadi, H., Li, H., & Roytershteyn, V. 2013, PhRvL, 110, 265004
Montag, P., Egedal, J., Lichko, E., & Wetherton, B. 2017, PhPl, 24, 062906
Northrop, T. G. 1963, The Adabatic Motion of Charged Particles No 21 (New York: Interscience)
Numata, R., & Loureiro, N. F. 2015, JPlPh, 81, 305810201
Oka, M., Ishikawa, S., Saint-Hilaire, P., Krucker, S., & Lin, R. P. 2013, ApJ, 764, 6
Oka, M., Krucker, S., Hudson, H. S., & Saint-Hilaire, P. 2015, ApJ, 799, 129
Shay, M. A., Haggerty, C. C., Phan, T. D., et al. 2014, PhPl, 21, 122902
Sironi, L., & Spitkovsky, A. 2014, ApJL, 783, L21
Stanier, A., Daughton, W., Le, A., Li, X., & Bird, R. 2019, PhPl, 26, 072121
Wang, H., Lu, Q., Huang, C., & Wang, S. 2016, ApJ, 821, 84
Werner, G. R., Uzdensky, D. A., Cerutti, B., Nalewajko, K., & Begelman, M. C. 2016, ApJL, 816, L8
Zank, G. P., Hunana, P., Mostafavi, P., et al. 2015, ApJ, 814, 137
Zank, G. P., le Roux, J. A., Webb, G. M., Dosch, A., & Khabarova, O. 2014, ApJ, 797, 28
Zhao, L.-L., Zank, G. P., Chen, Y., et al. 2019, ApJ, 872, 4
Zhao, L.-L., Zank, G. P., Khabarova, O., et al. 2018, ApJL, 864, L34
Zweibel, E. G., & Yamada, M. 2009, ARA&A, 47, 291